Available online at www.sciencedirect.com

ScienceDirect

Acta Materialia 92 (2015) 126–139

Acta MATERIALIA

www.elsevier.com/locate/actamat

The role of twinning deformation on the hardening response of polycrystalline magnesium from discrete dislocation dynamics simulations

Haidong Fan,[a,b,*] Sylvie Aubry,[c] Athanasios Arsenlis[c] and Jaafar A. El-Awady[a]

[a] *Department of Mechanical Engineering, Johns Hopkins University, Baltimore, MD 21218, USA*
[b] *Department of Mechanics, Sichuan University, Chengdu, Sichuan 610065, China*
[c] *Materials Science Division, Lawrence Livermore National Laboratory, Livermore, CA 94551-0808, USA*

Received 30 January 2015; revised 20 March 2015; accepted 24 March 2015

Abstract—The deformation of micro-twinned polycrystalline magnesium (Mg) was studied using three-dimensional discrete dislocation dynamics (DDD). A systematic interaction model between dislocations and $\{10\bar{1}2\}$ tension twin boundaries (TBs) was proposed and introduced into the DDD framework. In addition, a nominal grain boundary (GB) model based on experimental results was also introduced to mimic the GB's barrier effect. The current simulations show that tension TBs act as strong obstacles to gliding dislocations, and contribute significantly to the overall hardening response, while twin growth results in a softening effect. Therefore, the Mg concave stress–strain curve can be explained in terms of the competition between TB induced hardening and twin growth induced softening. At low strain levels, twin growth induced softening dominates and a decreasing hardening rate is observed in Stage-I. In Stage-II, the TB induced hardening dominates, which leads to an increasing hardening rate.

Keywords: Discrete dislocation dynamics; Dislocations; Twinning; Magnesium; Hardening

1. Introduction

With the increasing demand to reduce carbon dioxide emission, many efforts are directed toward reducing the structural weight of fossil fuel powered vehicles to increase their fuel efficiency. As the lightest structural metal (one-third lighter than aluminum), magnesium (Mg) and its alloys have been attracting a lot of attention in recent years for their potential use in automotive, aerospace and defense applications [1]. However, at present, the wide use of Mg alloys as a structural material is still challenging due to their poor room temperature formability. Owing to its hexagonal closed packed (hcp) lattice structure and low crystal symmetry, Mg cannot maintain sufficient independent slip modes to accommodate arbitrary deformation in polycrystalline materials at room temperature. Consequently, in addition to dislocations, twinning plays an important role in their plastic deformation. Therefore, it is vital to grasp a full understanding of the combined effects of dislocations, twinning, and their mutual interactions to address their role on the overall mechanical behavior of hcp materials [2].

Due to deformation twinning, the deformation of Mg and its alloys displays characteristics that are different than those commonly observed in face centered cubic (fcc) and body centered cubic (bcc) crystals. One common characteristic is that the true stress–strain curves of both single crystals [3,4] and polycrystalline [4,5] Mg display a concave shape. In addition, the stress–strain curve can be characterized by three distinct stages. In Stage-I a decreasing hardening rate is observed, followed by Stage-II with an increasing hardening rate, and finally a decreasing hardening rate in Stage-III [4,5]. Stage-I is generally associated with twinning-mediated plasticity in the form of twin nucleation and growth, leading to a decreasing hardening rate [6–8]. On the other hand, the progressive decrease in the work hardening rate in Stage-III is a result of post-saturation in the twin volume fraction leading to predominant dislocation-mediated plasticity [6,9]. In Stage-II, both dislocation slip and twinning are active and interact; however, the underlying mechanisms associated with the increasing hardening rate are still debated.

Jiang et al. [6] examined the microstructure evolution during AZ31 deformation, and observed that in Stage-II intersections between primary and secondary $\{10\bar{1}2\}$ tension twins result in significant grain refinement and subsequently an increasing hardening rate. On the contrary, Wang et al. [10] reported that the barrier effect of tension twin boundaries (TBs) weakens as twins coalesce during Stage-II, which undermines the suggested contribution from grain refinement. In addition, they suggested that the increasing hardening rate can be attributed to texture induced hardening. This is a result of the tension twin hard

* Corresponding author at: Department of Mechanical Engineering, Johns Hopkins University, Baltimore, MD 21218, USA; e-mail addresses: haidongfan8@foxmail.com; jelawady@jhu.edu

http://dx.doi.org/10.1016/j.actamat.2015.03.039
1359-6462/

Report Documentation Page

Form Approved
OMB No. 0704-0188

1. REPORT DATE	2. REPORT TYPE	3. DATES COVERED
2015		**00-00-2015 to 00-00-2015**

4. TITLE AND SUBTITLE	5a. CONTRACT NUMBER
The Role of Twinning Deformation on the Hardening Response of Polycrystalline Magnesium from Discrete Dislocation Dynamics Simulations	5b. GRANT NUMBER
	5c. PROGRAM ELEMENT NUMBER
6. AUTHOR(S)	5d. PROJECT NUMBER
	5e. TASK NUMBER
	5f. WORK UNIT NUMBER
7. PERFORMING ORGANIZATION NAME(S) AND ADDRESS(ES) **Johns Hopkins University ,Department of Mechanical Engineering ,Baltimore,MD,21218**	8. PERFORMING ORGANIZATION REPORT NUMBER
9. SPONSORING/MONITORING AGENCY NAME(S) AND ADDRESS(ES)	10. SPONSOR/MONITOR'S ACRONYM(S)
	11. SPONSOR/MONITOR'S REPORT NUMBER(S)

12. DISTRIBUTION/AVAILABILITY STATEMENT
Approved for public release; distribution unlimited

13. SUPPLEMENTARY NOTES

14. ABSTRACT

The deformation of micro-twinned polycrystalline magnesium (Mg) was studied using three-dimensional discrete dislocation dynamics (DDD). A systematic interaction model between dislocations and f10 12g tension twin boundaries (TBs) was proposed and introduced into the DDD framework. In addition, a nominal grain boundary (GB) model based on experimental results was also introduced to mimic the GB???s barrier effect. The current simulations show that tension TBs act as strong obstacles to gliding dislocations, and contribute significantly to the overall hardening response, while twin growth results in a softening effect. Therefore, the Mg concave stress???strain curve can be explained in terms of the competition between TB induced hardening and twin growth induced softening. At low strain levels, twin growth induced softening dominates and a decreasing hardening rate is observed in Stage-I. In Stage-II, the TB induced hardening dominates, which leads to an increasing hardening rate.

15. SUBJECT TERMS

16. SECURITY CLASSIFICATION OF:			17. LIMITATION OF ABSTRACT	18. NUMBER OF PAGES	19a. NAME OF RESPONSIBLE PERSON
a. REPORT	b. ABSTRACT	c. THIS PAGE			
unclassified	**unclassified**	**unclassified**	**Same as Report (SAR)**	**14**	

orientation, since its c-axis is nearly parallel to the loading axis. Knezevic et al. [7] showed that tension twins consume the entire grain before the end of Stage-II, and all the aforementioned twinning mechanisms cannot explain the peak strain hardening rate at the end of Stage-II. Instead, they suggested that this peak strain hardening rate may be attributed to the nucleation of compression twins in the tension twinned grains. Barnett et al. [5] observed the formation of low angle boundaries arising from the glissile-to-sessile transition of dislocations induced by twinning shear [11,12], which can also act as a source of hardening. Finally, de-twinning as a result of strong interactions between dislocations and twins was also suggested to contribute to the observed increasing strain hardening rate in Stage-II [13]. These conflicting proposed mechanisms indicate that there is no clear consonance yet regarding the mechanisms responsible for the increasing strain hardening rate in Stage-II.

In the past two decades, several computational methods have been developed to characterize dislocation-mediated plasticity. Of those, discrete dislocation dynamics (DDD) is one of the most efficient methods to capture dislocation-mediated plasticity at the micro scale. To date, several two-dimensional [14,15] and three-dimensional [16–19] DDD methods were proposed and used widely to study crystal size effects (e.g. [20–22]), grain size effects (e.g. [23–25]) and intermittency behavior (e.g. [26]). While most previous DDD studies have focused on fcc and bcc crystals, more recently several studies have been performed on hcp crystals. In particular DDD simulations of hcp materials have focused on dislocation junction formation and strength [27,28], orientation influence on the grain size effects [25], micro/nano-pillar plasticity [29,30], elastic anisotropy [31], and the role of plastic anisotropy on microcracking [32]. It should be noted that in these studies deformation twinning was not considered. Nevertheless, twinning plays an important and sometimes dominant role in the mechanical behavior of both single crystalline and polycrystalline Mg. As a result, DDD simulations not accounting for twinning may lead to inaccurate predictions of the mechanical behavior of hcp materials. This also indicates the importance and urgency of developing a dislocation–TB interaction model within the framework of DDD to account for deformation twinning.

As aforementioned, the deformation of Mg and its alloys is of great interest due to their numerous potential applications in industry. However, the mechanisms associated with their hardening response, mainly in Stage-II, are not well characterized. In order to address this, we propose a systematic interaction model between dislocations and $\{10\bar{1}2\}$ TBs, and integrate this model into 3D-DDD simulations. A simple grain boundary (GB) model, which agrees with experimental results, is also implemented. Using this complex DDD framework, the deformation of micro-twinned polycrystalline Mg is investigated. Specifically these simulations identify the influences of grain orientation, GBs, TBs and twin volume fraction on the deformation of Mg polycrystals.

2. Computational methods

In the following simulations, a cubic simulation cell is employed to model a representative grain in a bulk material, as shown schematically in Fig. 1(a), where periodic boundary conditions (PBCs) are imposed along all three directions. A twin lamella having a thickness l_t is introduced at the center of the grain with size l_g. Thus, the twin volume fraction is given by $f_t = l_t/l_g$. Here, only $\{10\bar{1}2\}$ tension twins are considered, as shown by the relative orientations of the grain and twin in Fig. 1(a). It has been shown experimentally that the number of twins per grain is proportional to the square of grain size, and the probability of having more than one twin per grain decreases considerably for grains having diameters less than 40 μm [33]. Thus, given the grain sizes modeled here, the current proposed simulation cell can be considered as a representative twinned grain in a bulk Mg polycrystal with grain size below 40 μm.

In Mg polycrystals, strain hardening can be attributed to three microstructural features: dislocations, GBs and TBs. In order to investigate their individual contributions, three additional simplified cubic simulation cells are considered, as shown in Fig. 1. In one case, only dislocations are accounted for in a single crystal cubic simulation cell with PBCs along all three directions. In another case, the contribution of GBs is accounted for in a polycrystal simulation cell in the absence of TBs. In this case, the six surfaces of the simulation cell are considered as representative GBs with PBCs along all three directions. Finally, the effect of TBs is accounted for in a twinned crystal simulation cell in the absence of GBs. Here, a twin lamella is inserted in the middle of the simulation cell and PBCs are employed along all three directions. It should be noted that these simulation cells are idealized, since twinning is typically observed experimentally in bulk single crystals and polycrystals. Nevertheless, these simulations can provide new insights into the individual contributions of dislocations, GBs and TBs on the hardening response of Mg.

In metals, screw dislocation cross-slip is an important mechanism for strain hardening [34] and creep behavior [35]. Therefore, a general cross-slip mechanism is utilized in the current simulations. Cross-slip of a screw dislocation is possible when more than one slip system share the same Burgers vector [36]. In particular $\langle a \rangle$ dislocations can cross-slip between basal, prismatic and pyramidal I planes, $\langle c \rangle$ dislocations between prismatic slip planes, and $\langle c + a \rangle$ dislocations between prismatic, pyramidal I and pyramidal II planes. Further details about the cross-slip mechanism used here can be found elsewhere [36].

In fully tension-twinned grains, compressive loading parallel to the c-axis, or tensile loading perpendicular to the c-axis, would promote compression twinning [7]. These compression twins appear always in a thin band shape with low volume fraction [7]. To model this effect, in a small number of simulations we also introduce a nominal compressive twin with a volume fraction of 0.05 in the center of the fully twinned grain. These compression TBs are assumed to be impenetrable to dislocations.

All current simulations were conducted using the 3D-DDD simulation code, ParaDiS [16]. All possible dislocation Burgers vectors and slip planes in hcp crystals, which are listed in Table 1, were accounted for in these simulations. It should be noted that according to the hcp lattice structure, slip of $\langle a \rangle$ dislocations and dislocations with Burgers vector $\boldsymbol{b}_t$ (i.e. twinning dislocations) on the $\{10\bar{1}2\}$ twinning planes are also possible. Thus, these dislocations are accounted for in the current simulations as well. The experimentally measured Peierls stresses for dislocations on the basal (0.52 MPa [37]), prismatic

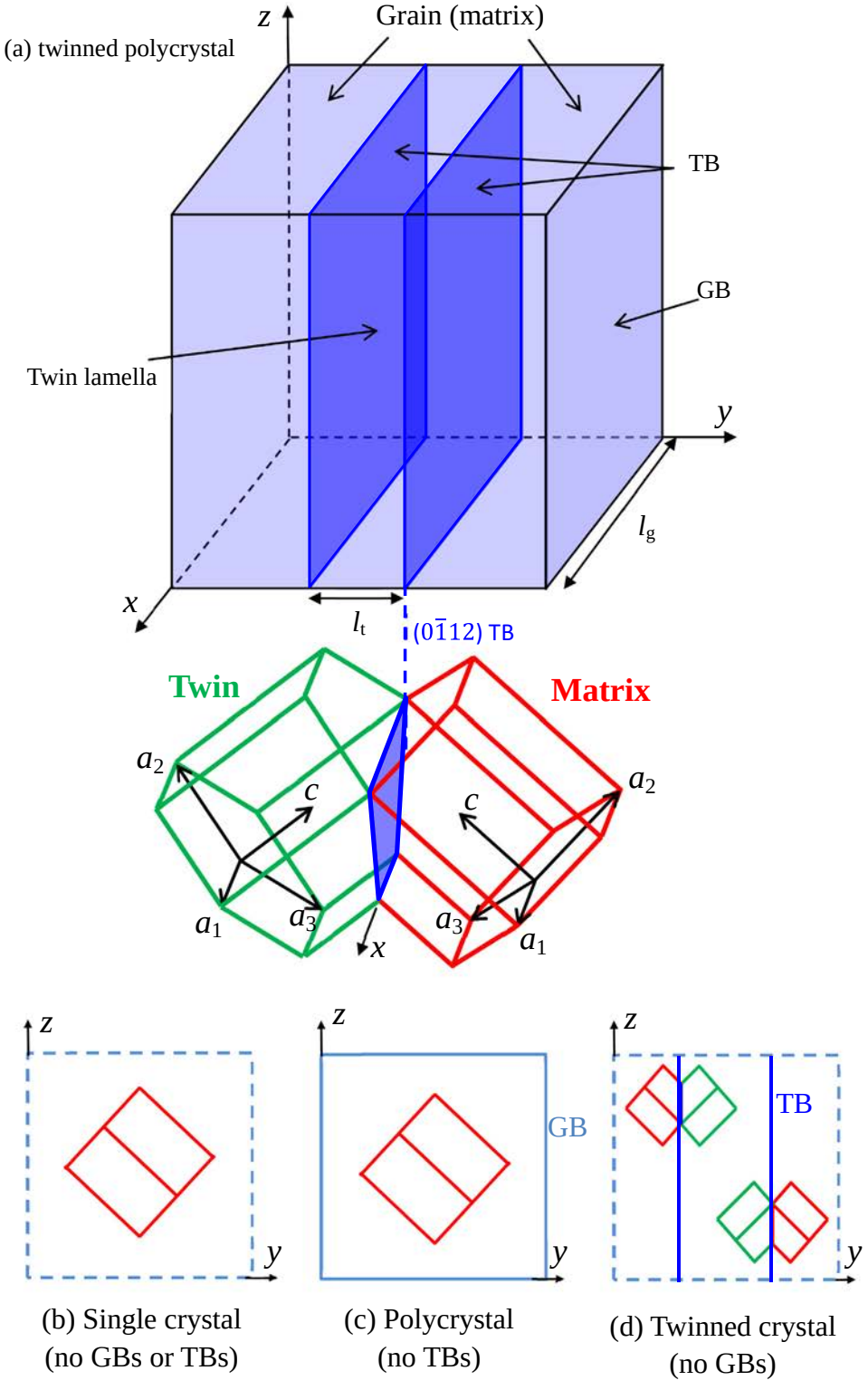

Fig. 1. Schematic of the four simulation cells, showing twin boundaries, grain boundaries, and orientations. (a) Twinned polycrystal with both GBs and TBs; (b) single crystal without GBs or TBs; (c) polycrystal without TBs; and (d) twinned crystal without GBs.

(39.2 MPa [38]), and pyramidal planes (105 MPa [39]) were introduced into the code. These values are also in good agreement with recent molecular dynamics (MD) calculations [40–43]. Basic Mg parameters used in the current simulations include: shear modulus, $G = 17$ GPa; Poisson ratio, $v = 0.29$; magnitude of $\langle a \rangle$ dislocation Burgers vector, $b = 0.325$ nm; axial ratio, $c/a = 1.6236$; and mass density, $\rho = 1738$ kg m^{-3}.

While most DDD simulations typically adopt a linear dislocation mobility law, recent MD simulations suggest that the dislocation mobility in Mg is nonlinear [41]. At low stress levels the dislocation velocity was shown to

Table 1. Slip systems introduced in the current DDD framework. The underlined four symbols indicate the slip systems of initial dislocations in the simulation cell.

Slip planes	Burgers vectors			
	$\langle a\rangle$ $\langle 11\bar{2}0\rangle$	$\langle c\rangle$ $\langle 0001\rangle$	$\langle c+a\rangle$ $\langle 11\bar{2}3\rangle$	$\mathbf{b}_t$ $\lambda[01\bar{1}1]^*$
Basal – $\{0001\}$	$\underline{\times}$			
Prismatic – $\{10\bar{1}0\}$	$\underline{\times}$	$\times$	$\times$	
Pyramidal I – $\{10\bar{1}1\}$	$\underline{\times}$		$\times$	
Pyramidal II – $\{11\bar{2}2\}$			$\underline{\times}$	
Twinning plane – $\{10\bar{1}2\}$	$\times$			$\times$

* $\lambda = \frac{|(c/a)^2-3|}{(c/a)^2+3}/2$.

increase linearly with the applied stress, and at higher stress levels the velocity also increases linearly but with a much smaller slope. Thus, in the current simulations we employ an MD fitted bi-linear relationship. The drag coefficients and transition velocities for the stress–velocity curve are listed in Table A1 in Appendix A. The upper limit to the dislocation velocity was set to be the shear wave velocity, $\sqrt{G/p}$. Furthermore, as a first approximation, the dislocation mobility and Peierls stress on the twinning plane were set equal to those on the pyramidal plane, since their precise values have not been reported in literature yet.

Uniaxial strain-controlled loading (compressive or tensile) with a constant strain rate of $\dot{\varepsilon} = 5000\ \mathrm{s}^{-1}$ was imposed in the current simulations. Due to the configuration symmetry along the x and z axes with respect to the twin lamella, the loading axis is confined within the yz plane. As a result, four representative loading directions denoted by y, z, yz and $y\bar{z}$, are considered. Loadings along the y and z directions are realized by imposing a constant strain rate $\dot{\varepsilon}_y = \dot{\varepsilon}$ and $\dot{\varepsilon}_z = \dot{\varepsilon}$ in the y and z directions, respectively. The yz loading is along a direction 45° from either the y or z axis, and is achieved by imposing the strain rate tensor:

$$\dot{\boldsymbol{\varepsilon}} = \dot{\varepsilon}\begin{bmatrix} -v & 0 & 0 \\ 0 & (1-v)/2 & (1+v)/2 \\ 0 & (1+v)/2 & (1-v)/2 \end{bmatrix} \tag{1}$$

Similarly, the $y\bar{z}$ loading is along a direction 45° from the y axis and 135° from the z axis, and is achieved by imposing the strain rate tensor:

$$\dot{\boldsymbol{\varepsilon}} = \dot{\varepsilon}\begin{bmatrix} -v & 0 & 0 \\ 0 & (1-v)/2 & -(1+v)/2 \\ 0 & -(1+v)/2 & (1-v)/2 \end{bmatrix} \tag{2}$$

Initially, Frank–Read (FR) dislocation sources were randomly distributed within the simulation cell (in both the matrix and the twinned region). The initial dislocation source density in all simulations was $\rho_{\mathrm{src}} = 5 \times 10^{12}\ \mathrm{m}^{-2}$, and the FR source length was $l_{\mathrm{src}} = 0.26\ \mu\mathrm{m}$. While dislocation slip on various slip planes is possible in hcp crystals as listed in Table 1, $\langle a\rangle$ dislocations on basal, prismatic and pyramidal I planes as well as $\langle c+a\rangle$ dislocations on pyramidal II planes play a predominant role in dislocation mediated plasticity of Mg [44,45]. Therefore, in the current simulations all dislocation sources were initially assigned to these four slip planes with equal numbers, which also agree with previous studies [25,46,47]. To account for possible statistical variations due to the random distribution of the dislocation sources, each simulation was repeated three times with different initial distributions.

2.1. Dislocation–twin boundary interaction model

To accurately model dislocation–TB interactions in DDD we first derive a set of physically based rules for these interactions from experimental observations and/or MD simulations. Price [48] first studied these interactions in Zinc and showed that an $\langle a_1\rangle$ dislocation, which intersects the TB in a screw character, can transmit through the TB without any remnants on the TB. On the other hand, $\langle a_2\rangle$ and $\langle a_3\rangle$ dislocations in the matrix can only be transmitted mutually through the TB by forming a $\langle c\rangle$ dislocation in the twinned crystal while leaving two twinning dislocations on the TB. Yoo and Wei [49] subsequently developed a set of dislocation–TB interaction scenarios for $\langle a\rangle$ and $\langle c+a\rangle$ dislocations based on geometric considerations of the hcp crystal structure. Electron microscope observations have shown good agreement with the Yoo and Wei model [49–52]. Furthermore, Yoo [53] performed a detailed analysis and proposed twenty six distinct types of interactions between three dislocation families and four most common twin boundaries in hcp crystals. In addition to these experimental observations, recent MD simulations showed that the dislocation–TB interactions are dependent on the loading direction. In particular, it was shown that $\langle a_1\rangle$ dislocations on the basal plane in the matrix can be transmitted to the basal plane in the twin, the prismatic plane in the twin, or the prismatic plane in the matrix depending on the direction of the applied load [54,55]. In addition, no residual or twinning dislocations were left on the TB, which agrees well with experimental observations. However, $\langle a_2\rangle$ and $\langle a_3\rangle$ dislocations were observed to introduce a twinning dislocation in the form of TB steps after absorption by the TB [56,57]. The subsequent motion of these twinning dislocations leads to TB migration, which agrees with the twin growth mechanism by twinning dislocations [56].

In the current model, two rules are specified to identify the reaction outcomes of a dislocation–TB interaction, in terms of twinning dislocations on the TB as well as Burgers vectors and slip planes of the transmitted dislocations in the twin. In particular, these rules are based on (a) geometric constraints, and (b) maximum power dissipation.

The geometric rule predicts the resulting dislocations and twinning dislocations. Accordingly, the systematic interaction scenarios of Yoo [53] between different dislocations (i.e. $\langle a\rangle$, $\langle c\rangle$ and $\langle c+a\rangle$) and the $\{10\bar{1}2\}$ TB were introduced into the DDD framework. It should be noted that in Yoo's model some peculiar dislocation reactions were proposed. In particular, $\langle c+a\rangle$ and $\langle c\rangle$ incident dislocations were proposed to be transmitted as dislocations with Burgers vectors $[5\bar{7}2\bar{3}]/6$ and $[\bar{1}100]$, respectively. However, these high lattice index dislocations

would not be stable because of their high Peierls stresses and core energies, and should be decomposed into more common dislocations having Burgers vectors with low lattice indexes. Our MD simulations (not presented here) show that a $[\bar{1}100]$ dislocation decomposes into two $\langle a\rangle$ dislocations such that $[\bar{1}100] \rightarrow [\bar{1}2\bar{1}0]/3 + [\bar{2}110]/3 = \langle a_2\rangle - \langle a_1\rangle$. Furthermore, simple geometric calculations show that $[5\bar{7}2\bar{3}]/6$ can be decomposed into 1.5 $\langle a\rangle$ and 0.5 $\langle c+a\rangle$ dislocations (i.e. $[5\bar{7}2\bar{3}]/6 \rightarrow [1\bar{2}10]/2 + [2\bar{1}\bar{1}\bar{3}]/6 = 1.5\langle a\rangle + 0.5\langle c+a\rangle$). Thus, in the current simulations, these low lattice index dislocations are defined instead.

The general dislocation decomposition proposed here is listed in Table A2 in Appendix A, in which all the possible incident dislocations from all slip planes are considered. All the resulting dislocation Burgers vectors and slip planes have low lattice index. The resulting slip planes were chosen to be tilt planes with respect to the incident plane. Thus, if a tilt plane does not exist, the dislocation is not allowed to penetrate (i.e. twisted boundaries are impenetrable). This geometric rule is analogous to that used for dislocation–GB interaction in DDD simulations of fcc polycrystals [14,23,26].

While for most incident dislocations this geometric rule is sufficient to identify the transmitted dislocation planes, this is not the case for incident $\langle a_1\rangle$ dislocations, which intersect the TB in a screw configuration. In this case, six potential tilt planes in the twin exist. Serra et.al [54] showed from MD simulations that depending on the direction of the applied load a matrix $\langle a_1\rangle$ dislocation on a basal plane can be transmitted to the twin basal plane, twin prismatic plane, or reflected back into the matrix on a prismatic plane. In these simple pure shear stress simulations, the resulting slip plane with the largest resolved shear stress was typically the one with the highest dislocation mobility. However, in the current DDD simulations, the stress field is always complex. In addition, since the Peierls stresses and mobility laws are strongly dependent on the slip system under consideration, thus, the plane with largest resolved shear stress does not necessarily produce the highest dislocation mobility. To account for all these factors, the most favorable plane is chosen to be the one that would result in the largest power dissipation [16]:

$$P = \sum \boldsymbol{F}_j \boldsymbol{V}_j \tag{3}$$

where $\boldsymbol{F}_j$ and $\boldsymbol{V}_j$ are the force and velocity of the jth transmitted dislocation.

It should be noted that in the current simulations, plasticity associated with TB migration or twin growth will not be accounted for due to the complexities of tracking an evolving boundary within the framework of DDD.

2.2. Dislocation–grain boundary interaction model

For the representative grain model with PBCs in all three directions, shown in Fig. 1, the orientation of each grain in the bulk is identical, which corresponds to a strong basal texture in polycrystalline Mg. However, the misorientation between the a-axes in neighboring grains is not accounted for here. Nevertheless, in the current simulations, the GB is introduced as an artificial interface/barrier to dislocation motion. As dislocations approach the GB they will be trapped. As a result, subsequent dislocations are piled up at the GB, leading to increasing the shear stress on the leading dislocation. Once this shear stress exceeds the GB strength, the leading dislocation can be transmitted into neighboring grains. This approximation was successfully adopted by DDD simulations of polycrystalline materials [25,58]. The GB transmission strength is largely governed by the misorientation angle, θ_{mis}, which can be approximated as $\tau_{GB} = 2G\sin^2(0.5\theta_{\mathrm{mis}})$ [14,23,26]. The effect of the misorientation angle on the stress–strain response from our DDD simulations in the absence of twinning is shown in Fig. 2. In these simulations the grain size was $l_g = 0.81$ μm, and a compressive loading along the y-axis was imposed, which produces a predominant basal slip deformation. An experimental stress–strain curve of a 0.8 μm grained Mg alloy under a similar loading condition [59] is also shown. It is clear that a misorientation angle of $\theta_{\mathrm{mis}} = 15°$ (i.e. GB strength $\tau_{\mathrm{GB}} = 580$ MPa) agrees well, in terms of the yield strength, with this experimental result, and thus in all subsequent simulations this GB strength is chosen.

3. Results and discussions

3.1. Hardening response of single crystals, polycrystals and twinned crystals

Here, the three simplified simulation cells shown in Fig. 1(b–d) are employed to study the individual contributions of dislocations (i.e. single crystals), GBs (i.e. polycrystals with no twins) and TBs (i.e. twinned crystals) on the hardening response of Mg. All the simulation cells have an edge-length $l_g = 1.3$ μm, and in the simulations of twinned crystals the twin thickness is $l_t = 0.5l_g$. Fig. 3 shows the stress–strain responses under different loading orientations from the three simulation cells. Fig. 4 shows the contours of the effective plastic strain at the end of each simulation, from which the slip traces can be identified. It is observed that the responses of single crystals loaded along the y and z directions (black curves in Fig. 3) are identical. These two loading directions make angles

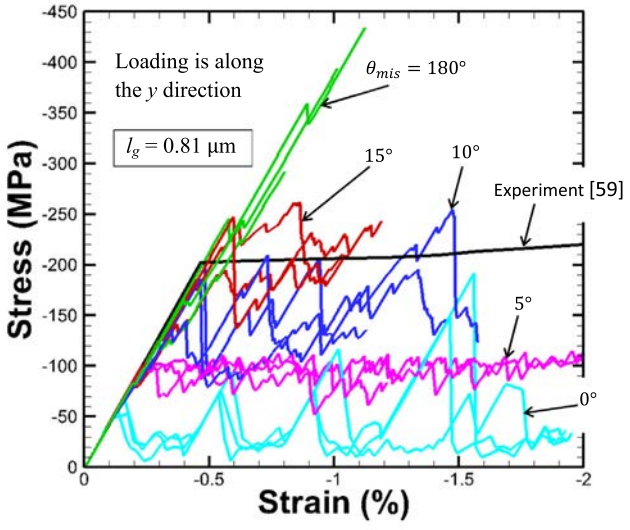

Fig. 2. Engineering stress–strain responses for different misorientation angles. Experimental result from [59] is also shown for comparison.

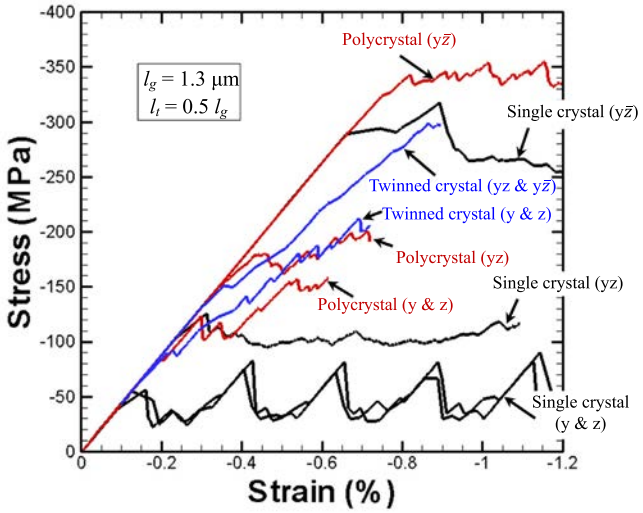

Fig. 3. Engineering stress–strain responses of single crystals, polycrystals and twinned crystals under different loading directions. Simulation cell dimensions are $l_g = 1.3$ μm, and $l_t = 0.65$ μm.

46.85° and 43.15°, respectively, with respect to the basal plane leading to predominant basal slip, as shown in Fig. 4(a), since the Schmid factor on these planes is maximum. The low yield stresses for these two loading orientations are mainly governed by the low Peierls stress and high dislocation mobility on the basal plane. On the other hand, loadings along the yz and $y\bar{z}$ directions lead to higher yield points. The yz direction is almost perpendicular to the c-axis, and plasticity is mediated by prismatic $\langle a \rangle$ dislocation slip (see Fig. 4(b)). Furthermore, the $y\bar{z}$ loading is 1.85° away from the c-axis, which leads to predominant $\langle c + a \rangle$ slip on pyramidal II planes (see Fig. 4(c)). As expected, the yield stress for loading along the $y\bar{z}$ direction is the highest since pyramidal slip is the hardest slip mode. It is also observed from Fig. 3 that regardless of the loading directions, all single crystals results exhibit weak strain hardening response in the absence of GBs or TBs up to 1% strain for this selected small periodic simulation cell.

Fig. 3 also shows the predicted stress–strain responses of polycrystals loaded in four different orientations (red curves). These simulations show that GBs lead to a significant rise in the crystal strength as compared to single crystal simulations. In particular, the yield strength increases by 208% for y and z loadings (basal slip), by 70% for yz loading (prismatic slip), and by 19% for $y\bar{z}$ loading (pyramidal slip), which are directly linked to the GB's barrier effect. From the contour maps in Fig. 4(d–f) the deformation modes are observed to be similar to those from single crystal simulations. In addition, higher strain hardening rates are observed in all simulations with GBs (i.e. the mean values from three realizations with different initial dislocation distributions are 15.5 GPa for basal, 8.2 GPa for prismatic and 5.4 GPa for pyramidal slips). The orientation dependence of the hardening rate is a result of the anisotropy in slip modes and Peierls stresses in Mg. Since basal slip is a single slip orientation (Fig. 4(d)), many dislocations pile up at the GBs, which lead to a strong back stress and a high strain hardening rate. For the prismatic and pyramidal slip orientations (Fig. 4(e–f)), plasticity is mediated by multi-slip, resulting in fewer dislocation pileups and lower strain hardening rates at the same strain levels.

Finally, the twinned crystals responses are shown by blue curves in Fig. 3. A twin lamella of thickness $l_t = l_g/2$ is introduced at the center of the simulation cell. For these simulations, only two unique loading directions exist. The y and z loading directions share the same stress–strain response and deformation modes in the matrix and twinned regions, while yz and $y\bar{z}$ loading directions share another one. The hardening rates for the y and yz loading directions are 20.4 GPa and 26.6 GPa, respectively, for deformation up to 0.8% strain. These rates are significantly higher than those observed from the polycrystal simulations. Fig. 4(g) shows the contours of the effective plastic strain for loading along the y direction. Dislocation slip is predominant on basal planes in both the matrix and the twin. Some slip traces are observed to be fully blocked in the twin or matrix, which is consistent with the high hardening rate observed in Fig. 3. On the other hand, some traces are connected across the TB, forming a long zigzag trace from basal planes in the matrix to basal planes in the twin. These observations are in qualitative agreement with experimental observations [49,50]. Furthermore, Fig. 4(h) shows a different deformation response during loading along the yz direction. Plasticity here is confined in the matrix since the twin is in a much harder orientation (pyramidal slip) as compared to the softer orientation of the matrix (prismatic slip).

In order to identify the effects of TBs on the hardening rate, the dislocation configurations from the twinned crystal simulations in both loading directions are shown in Fig. 5. For simulations with loading along the y direction, it is observed that many parallel dislocations pile up against the TB as shown in Fig. 5(a) by straight dislocations (red in the matrix and green in the twin). In this case, all the piled up dislocations in the matrix and twin are basal $\langle a_2 \rangle$ and $\langle a_3 \rangle$ dislocations, since the Schmid factor for $\langle a_1 \rangle$ dislocation is zero. According to the dislocation–TB interaction model shown in Table A2, these dislocations should decompose as follows

$$\langle a_2 \rangle \text{ or } \langle a_3 \rangle \rightarrow 0.5\langle c + a \rangle + \boldsymbol{b}_t \tag{4}$$

Thus, when the first dislocation (incident dislocation $\boldsymbol{b}_i$) arrives at the TB, it decomposes into one half $\langle c + a \rangle$ dislocation (a sessile residual dislocation $\boldsymbol{b}_r$ on the TB) and a twinning dislocation ($\boldsymbol{b}_t$), as shown in Fig. 5(a1). This decomposition is similar to that reported by MD simulations [55–57] and predicted experimentally [49,50]. While the Schmid factor on the TB is zero, the twinning dislocation is observed to glide away on the TB, as shown in Fig. 5(a2), due to the repulsive force between the residual dislocation and twinning dislocation. This residual dislocation also has a repulsive interaction with subsequent incident dislocations, which contributes to the dislocations pileup near the TB (see Fig. 5(a2)). With the increasing applied stress and number of pileup dislocations, the shear stress acting on the new leading incident dislocation in the pileup increases remarkably, and overcomes the repulsive interaction with the residual dislocation on the TB. Thus, the new incident dislocation would reach the TB and then decompose into another one half $\langle c + a \rangle$ dislocation and a twinning dislocation. Therefore, an integrated $\langle c + a \rangle$ dislocation can subsequently be emitted into the twinned crystal from the TB, as shown in Fig. 5(a3). This is

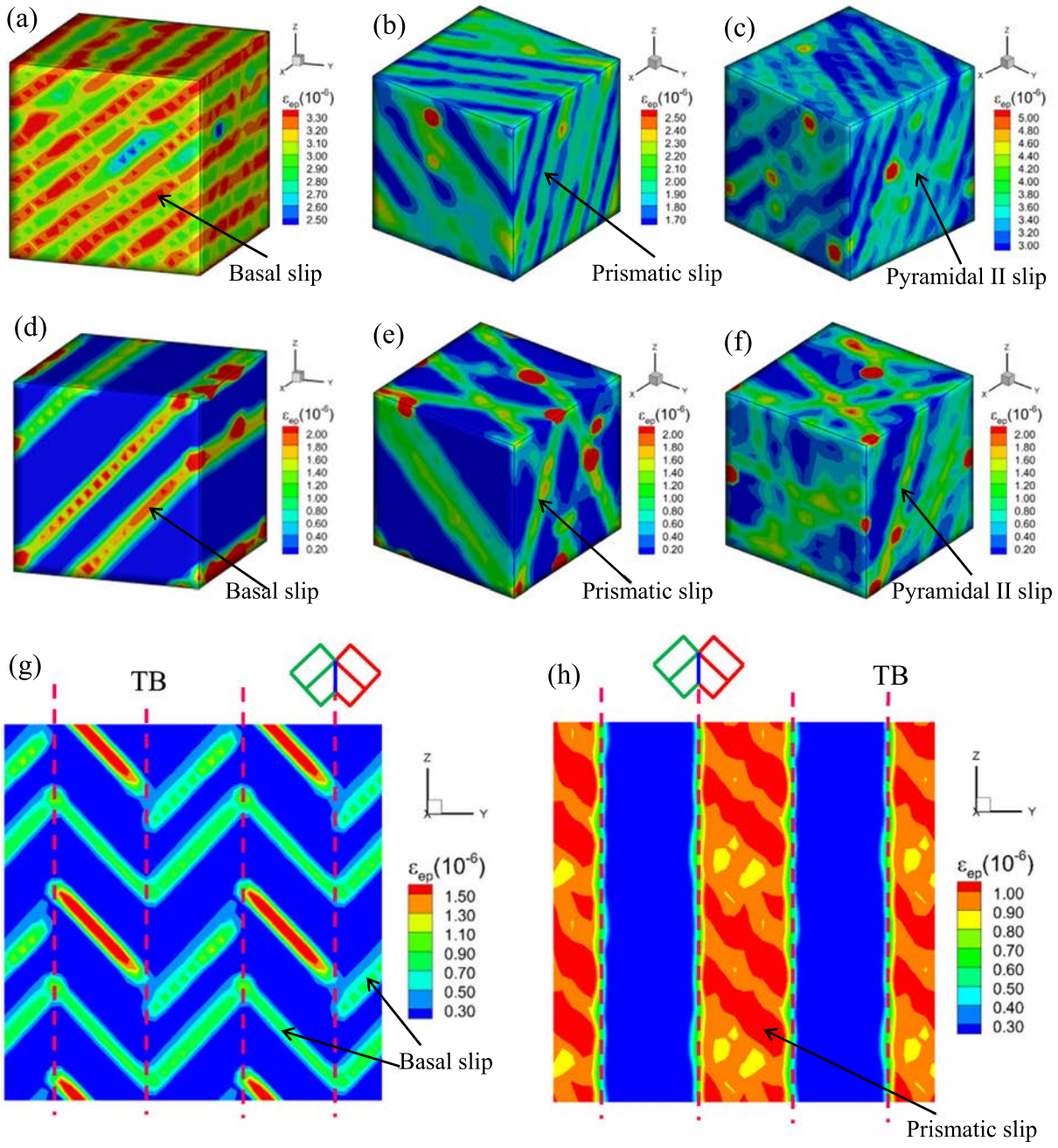

Fig. 4. Contours of effective plastic strain for: single crystals with loading in the (a) y, (b) yz, (c) $y\bar{z}$ directions; polycrystals with loading in the (d) y, (e) yz, (f) $y\bar{z}$ directions; and twinned crystals with loading in the (g) y, (h) yz directions. In (g) and (h), the image is a quad-duplicate of the original contour.

consistent with experimental observations [50,51]. As further dislocations reach the TB, the same decomposition processes would repeat. Finally, it should be noted that while dislocation transmission across the TB is observed in the current simulations, it occurs only at high local stress levels due to heavy dislocation pileups, as shown in Fig. 5(a4). This is one possible reason for the strong barrier effect of the TB based on the current proposed dislocation–TB interaction model.

On the other hand, during loading along the yz direction two dense dislocation networks are observed on the TBs (see Fig. 5(b)). Fig. 5(b1) shows that the network consists of two intersecting sets of parallel straight dislocations, and a group of curved dislocations. As stated previously, during loading along the yz direction, plasticity is accommodated by prismatic slip in the matrix. According to Eq. (4), the straight dislocations are half $\langle c+a\rangle$ residual dislocations, resulting from the incident prismatic $\langle a\rangle$ dislocations. The angle between the intersecting sets is 45.7°, which is the angle between the intersection lines of two prismatic planes on the TB. Furthermore, the curved dislocations are twinning dislocations, which glide

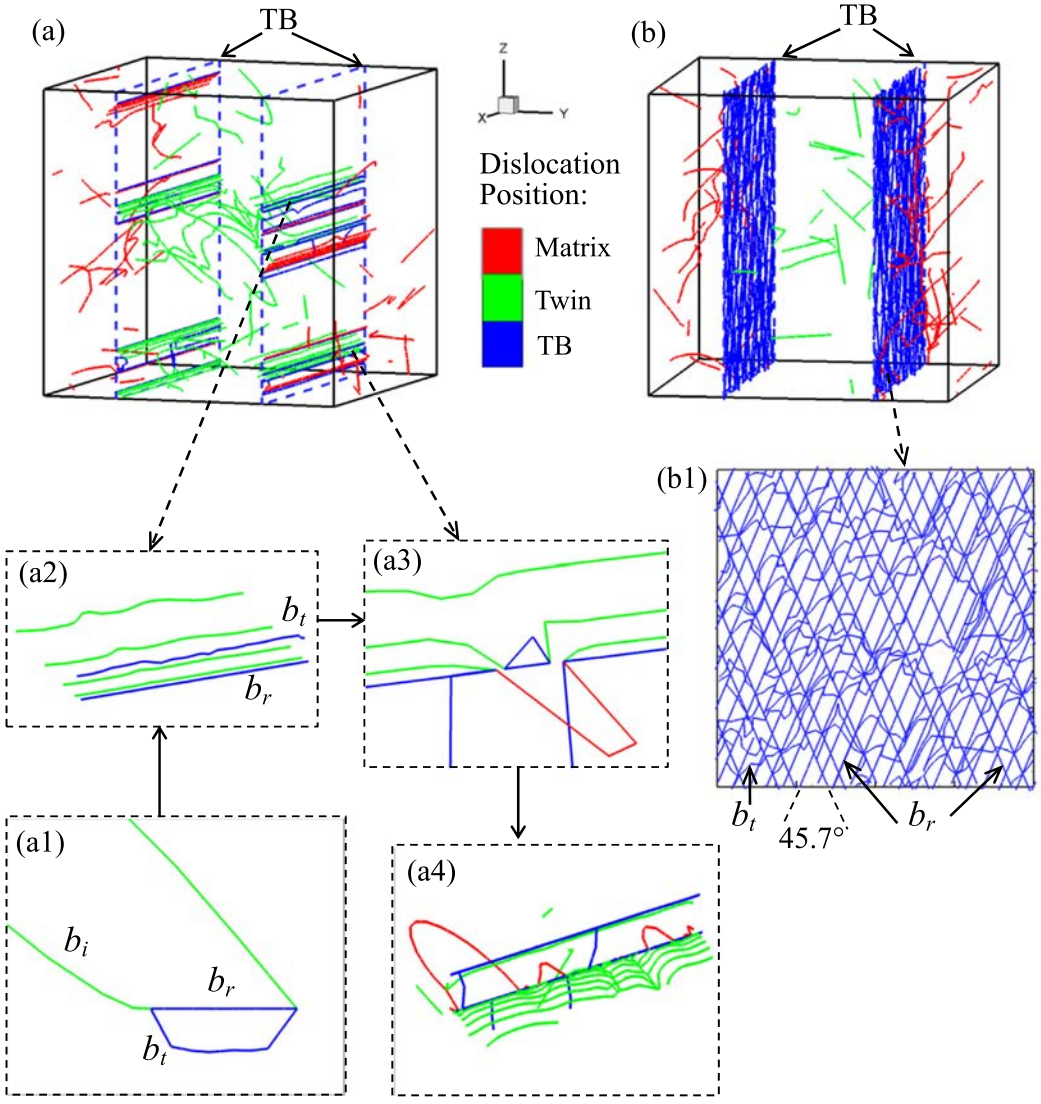

Fig. 5. Dislocation configurations in twinned crystals loaded in the (a) *y* and (b) *yz* directions. The inserts (a1) through (a4) and (b1) show dislocation–TB interaction details.

on the TB, since the Schmid factor is nonzero for this orientation.

As shown in Fig. 4(g), loading along the *y* direction is a single slip orientation since plasticity is accommodated by basal slip only. Thus, plasticity is confined to distinct planes and many dislocation pileups would be expected at the TBs (see Fig. 5(a)). On the other hand, loading along the *yz* direction leads to multi-slip deformation on prismatic planes. Subsequently, the contour of effective plastic strain in the matrix is uniform, as seen in Fig. 4(h), and few dislocation pileups are expected at the TBs (Fig. 5(b)) for the same strain level. It should be noted that prismatic slip during *yz* loading induces a higher hardening rate than basal slip during *y* loading, which seems contradictory to the hardening in Mg polycrystals as previously discussed. In fact, this is a result of the hard orientation (pyramidal slip) of the twin with respect to the *yz* loading axis, in which almost no plastic deformation is observed (Fig. 4(h)). Furthermore, in the *yz* loading the Schmid factor on the TB plane is high, leading to the glide of many twinning dislocations. This would subsequently contribute greatly to TB motion and twin growth [56,57], in agreement with experiments oriented for compressive loading perpendicular to the *c*-axis [6,8].

The current DDD simulations provide direct evidence of the three popular hardening mechanisms that are usually attributed to twinning in Mg and its alloys: (a) Hall–Petch induced hardening due to grain refinement by the evolving twins [9,60,61]; (b) Basinski mechanism: glissile-to-sessile transformation of dislocations due to the twinning shear [11,12]; and (c) texture hardening induced by the hard orientation in the twins [10,12]. Fig. 5(a) and (b) shows many sessile residual dislocations remain on the TB, which agrees well with the Basinski mechanism. The TBs also act as strong obstacles to dislocation motion, inducing grain refinement hardening. In addition, the absence of plasticity in the twinned region (see Fig. 4(h)) clearly demonstrates the hardening induced by the lattice orientation of the twins.

3.2. Hardening response of twinned polycrystals

To identify the collective contribution of dislocations, GBs and TBs on the hardening response of Mg, in this subsection the deformation of twinned polycrystals is investigated. In the following simulations the grain size is kept constant at $l_g = 1.3$ μm and the twin size, l_t, is varied to address the effect of twin volume fraction. Tension twinning has been reported experimentally to be facilitated by compression perpendicular to the c-axis, or tension parallel to the c-axis [6,8]. These correspond to the yz compressive loading and $y\bar{z}$ tensile loading, respectively.

The engineering stress–strain responses for different twin volume fractions ($f_t = l_t/l_g$) under yz compressive loading are shown in Fig. 6(a). The case of $f_t = 0.0$ corresponds to a polycrystal prior to twinning, while $f_t = 1.0$ corresponds to a fully twinned polycrystal. It is clear that the yield stress increases with increasing twin volume fraction, until it reaches a maximum at $f_t = 0.7$. The inset in Fig. 6(a) shows that dislocation activity in the matrix contributes mostly to the overall plastic deformation for $f_t < 0.7$. Subsequently, an increasing twin volume fraction results in reducing the matrix volume, which in turn results in increasing the yield stress of the crystal. Furthermore, the case of $f_t = 1.0$ indicates that the yield stress for the twin orientation is about 350 MPa. Thus, for a volume fraction $f_t > 0.5$, once the yield stress exceeds 350 MPa, dislocation slip in the twin begins to contribute to the overall plastic deformation. For $f_t > 0.7$, the overall plastic deformation is mainly accommodated by dislocation slip in the twin, since fewer dislocation sources would be present in the smaller matrix region. Therefore, the yield stress decreases with further increase in the twin volume fraction.

In a fully twinned grain (i.e. $f_t = 1.0$), the c-axis is close to the yz compressive loading direction, which is an orientation that would promote compression twinning. Knezevic et al. [7] observed compression twins and double twins in such oriented grains. These compression twins always appear in a thin band shape having a low volume fraction, and it was suggested that this contributes to the peak hardening rate in Stage-II [7]. To model this, here, we introduced a nominal compressive twin with a volume fraction of 0.05 in the center of the fully twinned grain. In the current simulations these compression TBs are assumed to be impenetrable to dislocations. To keep the notation consistent, this case is denoted by $f_t = 1.05$. Fig. 6(a) shows that the volume fraction of $f_t = 1.05$ results in the highest yield stress, which supports the potential contribution of compression twins on hardening in Mg polycrystals after tension twin saturation.

The stress–strain responses as a function of tension twin volume fraction under $y\bar{z}$ tensile loading are plotted in Fig. 6(b). The yield stress displays a different character than that of yz compressive loading. The yield stress is observed to increase with increasing twin volume fraction up to $f_t = 0.2$. Subsequently, for a volume fraction $0.2 \leqslant f_t \leqslant 1.0$, the yield stress continuously decreases. This can be explained as follows. Under $y\bar{z}$ tensile loading, the matrix c-axis is close to the loading direction, thus, the matrix is oriented for a hard deformation mode (i.e. pyramidal slip orientation). For $f_t \leqslant 0.2$, the plastic deformation is mainly mediated by dislocations activity in the matrix. Thus, as the twin volume fraction increases the matrix volume decreases, leading to an increasing yield stress. For

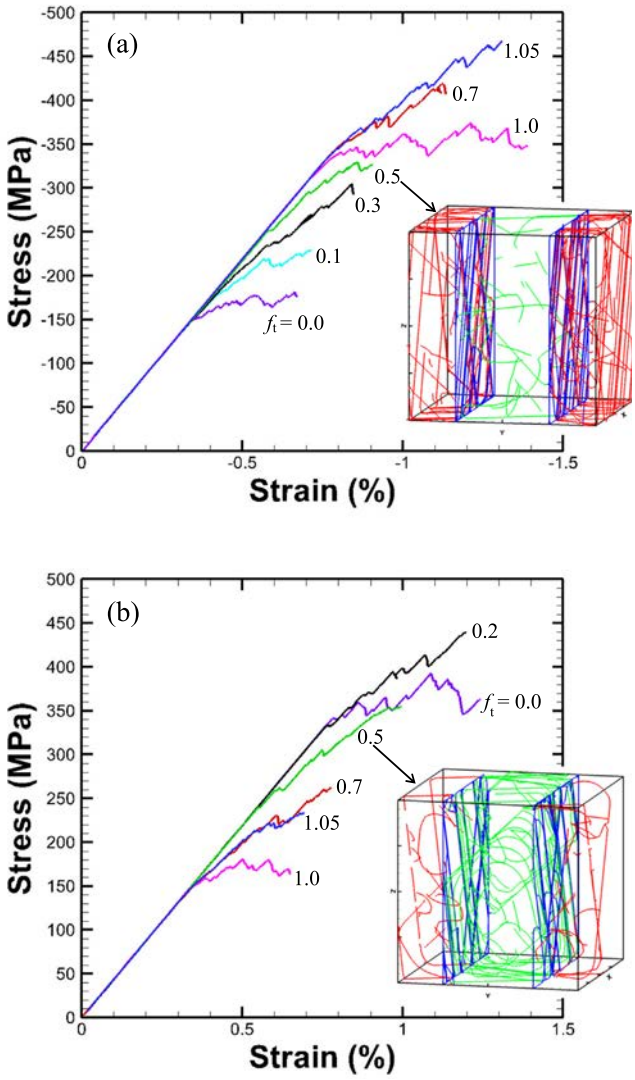

Fig. 6. Engineering stress–strain responses of twinned polycrystals having different twin volume fractions under (a) yz compressive and (b) $y\bar{z}$ tensile loadings.

$f_t > 0.2$, the plastic deformation is gradually dominated by dislocation slip in the twin, which is in a soft orientation (i.e. prismatic slip orientation), as shown by the inset in Fig. 6(b). As a result, the yield stress decreases with increasing twin volume fraction.

It should be noted that the initial dislocation densities in all simulations of different twin volume fractions shown in Fig. 6 are the same. However, in real Mg crystals, the twin volume fraction increases with increasing strain, and it might be expected that subsequently the dislocation density would also increase. These increases in the dislocation density are not accounted for in the current study due to computational difficulties associated with the increasing number of degrees of freedom with increasing dislocation density.

Fig. 7 shows the hardening rate due to dislocation slip, θ_S, as a function of twin volume fraction for the two loading directions. These rates are computed from a linear fit of the stress–strain curves in Fig. 6 above a plastic strain of $\varepsilon_p = -0.05\%$. It is observed that the dislocation slip induced hardening rate during yz loading increases with

increasing twinning volume fraction for $f_t \leqslant 0.3$, then decreases for $0.3 \leqslant f_t \leqslant 1.0$, as shown in Fig. 7(a). Subsequently, the hardening rate increases again with the introduction of a compression twin with 0.05 volume fraction in the fully twinned grain (i.e. $f_t = 1.05$). On the other hand, the dislocation slip induced hardening rate during $y\bar{z}$ tensile loading from the current DDD simulations is shown in Fig. 7(b). Similar trends to the yz compressive loading are observed, with θ_S increasing for $f_t \leqslant 0.4$, then decreasing for $0.4 \leqslant f_t \leqslant 1.0$. Furthermore, for the case of fully twinned grains with compressive twinning at a volume fraction of 0.05 (i.e. $f_t = 1.05$), the dislocation slip induced hardening rate is observed to subsequently increase, which agrees well with experimental predictions [7].

It should be noted that only dislocation-mediated plasticity is accounted for in the current DDD simulations. Under actual experimental conditions, plastic deformation is mediated by both dislocation slip and twin growth (TG), with twin growth playing a major role especially at low strain levels. Thus, the contribution from twinning plasticity must be taken into account. Accordingly, the overall hardening rate, θ, can be decomposed into a contribution induced by dislocation slip and a contribution induced by twin growth such that:

$$\begin{aligned}\theta &= \frac{d\sigma}{d\varepsilon} = \frac{d\left(E\left(\varepsilon - \varepsilon^p_{\text{slip}} - \varepsilon^p_{\text{twin}}\right)\right)}{d\varepsilon} \\ &= \left(E - \frac{d\left(E\varepsilon^p_{\text{slip}}\right)}{d\varepsilon}\right) + \left(-\frac{d\left(E\varepsilon^p_{\text{twin}}\right)}{d\varepsilon}\right) = \theta_s + \theta_{\text{TG}}\end{aligned} \tag{5}$$

Here, θ_{TG} is the hardening rate induced by twin growth only, and can be computed from the twin volume fraction [8] such that

$$\theta_{\text{TG}} = -\frac{d\left(E\varepsilon^p_{\text{twin}}\right)}{d\varepsilon} = -E\bar{m}\gamma_{\text{twin}}\frac{df_t}{d\varepsilon} \tag{6}$$

where $\bar{m}$ and γ_{twin} are the average Schmid factor of the twin variants and characteristic twinning shear, respectively. For $\{10\bar{1}2\}$ tension twins in Mg and its alloys, $\gamma_{\text{twin}} = 0.13$, while $\bar{m} = 0.437$, and 0.499 for yz compressive loading and for $y\bar{z}$ tensile loading, respectively [8].

For comparison with experiments, the dislocation slip induced hardening rates, θ_S, as measured from AZ31 polycrystals experiments under yz compressive, and $y\bar{z}$ tensile loadings [8] are also shown in Fig. 7. It is observed that the shape of the dislocation slip induced hardening rate, θ_S, from DDD simulations is in qualitative agreement with the experimental measurements, indicating that the DDD simulations are capable of capturing the main deformation mechanisms in Mg polycrystals. However, the experimental curves show higher hardening rates than the current DDD simulations. This difference can be attributed to two main reasons: (1) the experiments are performed on AZ31 polycrystals having a high density of second phase particles [29], while the simulations are performed on pure Mg polycrystals; (2) the initial dislocation density in the simulations is always fixed at $\rho_{\text{src}} = 5 \times 10^{12}\ \text{m}^{-2}$ for all modeled twin volume fractions, while in the experiments the dislocation density is expected to continuously increase with increasing twin volume fraction or applied strain. These differences between the simulation conditions and the experiments suggest that the dislocation-mediated hardening rate as measured experimentally will be higher than those predicted from the current DDD simulations.

In order to compute the twin growth induced hardening rate θ_{TG} through Eq. (6), the twin volume fraction reported experimentally from six different groups [6–8,62–65] for these two loading paths is plotted in Fig. 8 as a function of the applied strain. It is important to note that the twin volume fraction as a function of strain has been reported in literature to be independent of grain sizes [66], which agrees well with Fig. 8 for grain sizes 10–107 μm. Through this, the twin growth induced hardening rate, θ_{TG}, can be numerically computed from Eq. (6) based on the results shown in Fig. 8.

Finally, Fig. 9 shows the dislocation slip induced hardening rate, θ_S, as predicted from DDD, the twin growth induced hardening rate, θ_{TG}, as predicted from Fig. 8, and the overall hardening rate, $\theta = \theta_S + \theta_{\text{TG}}$, for the two simulated loading paths. For the yz compressive loading, the experimentally measured θ_{TG} is always negative and continuously increases with increasing twin volume fraction, as shown in Fig. 9(a). Furthermore, two stages can be identified from the overall hardening rate θ: (a) decreasing hardening rate for twin volume fraction $f_t \leqslant 0.1$; and (b)

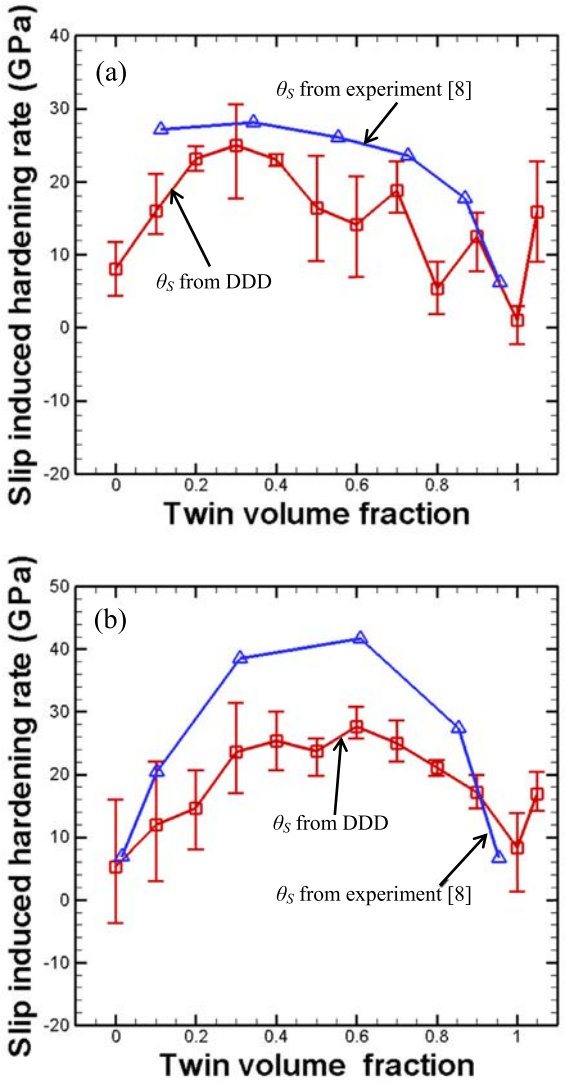

Fig. 7. Slip induced hardening rate θ_S as a function of twin volume fraction under (a) yz compressive and (b) $y\bar{z}$ tensile loadings.

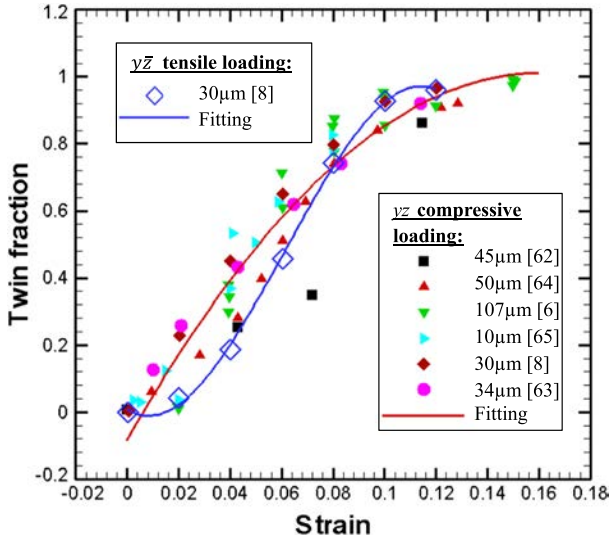

Fig. 8. Experimentally reported tension twin volume fraction in AZ31 with different grain sizes as a function of strain in two different loading paths. The best polynomial fitting curves, $f_t = -42.0\varepsilon^2 + 13.6\varepsilon - 0.083$ for yz compressive loading (perpendicular to c-axis), and $f_t = -1650.6\varepsilon^3 + 303.4\varepsilon^2 - 4.9\varepsilon + 0.00817$ for $y\bar{z}$ tensile loading (parallel to c-axis), are also shown.

increasing hardening rate for $f_t > 0.1$. These two stages mimic the experimentally reported Stage-I and Stage-II [6–8,64]. In addition, for $f_t = 1.05$ (i.e. compression twins in fully twinned grains), the highest hardening rate is achieved. This indicates that compression twins in the fully tension-twinned grains can be attributed to the peak hardening rate in Stage II, which agrees well with experimental results [7]. It should be noted that the total hardening rate is mainly negative, because the dislocation slip induced θ_S computed in current DDD simulations is lower than that measured in experiments, as clearly shown in Fig. 7.

As previously mentioned, there are at least three sources contributing to strain hardening in Mg polycrystals, including dislocation forest hardening, GBs induced hardening, and TBs induced hardening, which all contribute to θ_S. In Section 3.1, the dislocation forest hardening effect for single crystals was observed to be weak (see Fig. 3). Furthermore, GBs do produce considerable hardening, however, this contribution does not change with increasing twin volume fraction. Therefore, the variations in θ_S as a function of twin volume fraction are largely induced by the TBs, also conveying TBs produce a hardening effect on the overall response. On the other hand, the experimentally measured twin growth induced hardening rate, θ_{TG}, is always negative, as shown in Fig. 9(a), indicating twin growth produces a softening effect in the presence of dislocation slip. As a result, the two stages in the overall hardening rate, θ, can be explained by the competition between TB induced hardening and twin growth induced softening. In Stage-I, the twin growth induced softening dominates, so a decreasing overall hardening rate is seen. In Stage-II, both the TB induced hardening and twin growth induced softening decline, but the latter declines more rapidly, leading to a decreasing overall hardening rate.

On the other hand, Fig. 9(b) shows the hardening rates during $y\bar{z}$ tensile loading, in which identical phenomenon to the yz compressive loading is observed. The overall hardening rate θ displays two distinct stages, which are similar to

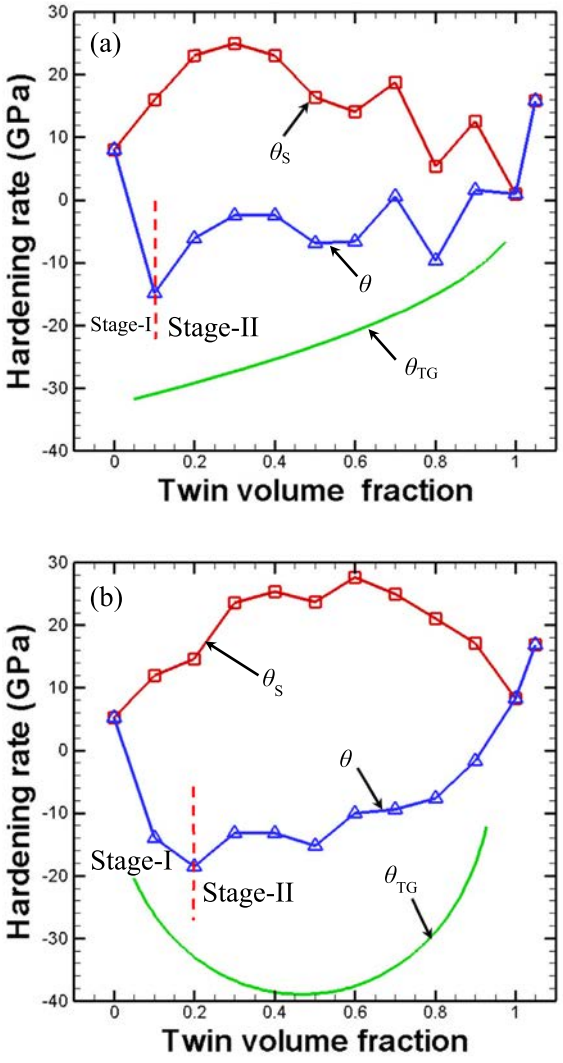

Fig. 9. Hardening rate as a function of twin volume fraction for (a) yz compressive loading and (b) $y\bar{z}$ tensile loading.

yz compressive loading and experimental observations [8,64]. Again, the case of fully twinned grains with compressive twinning at a volume fraction of 0.05 (i.e. $f_t = 1.05$) yields the peak hardening rate in Stage II, in good agreement with experimental observations [7]. These two stages can also be interpreted based on the competition between TB induced hardening and twin growth induced softening.

4. Conclusions

In this work, a systematic interaction model between dislocations and $\{10\bar{1}2\}$ TBs was proposed. In this model all the possible incident dislocations were taken into account. In order to mimic the GB strengthening, a nominal GB model agreeing with experimental results was proposed. Both the TB and GB models were introduced into the DDD framework to study the mechanical behavior of a representative twinned Mg grain. It was shown that TBs are strong obstacles to dislocation glide, and play a dominant role in the hardening response. On the other hand, the plastic deformation induced by twin growth produces a softening effect. Therefore, a competition exists

between TB induced hardening and twin growth induced softening. This competition results in the concave stress–strain curve. At low strain levels, the twin growth induced softening dominates, leading to a decreasing hardening rate in Stage-I. In Stage-II, the hardening effect dominates, which leads to an increasing hardening rate.

Acknowledgements

This research was sponsored by the Army Research Laboratory (#W911NF-12-2-0022). The views and conclusions contained in this document are those of the authors and should not be interpreted as representing the official policies, either expressed or implied, of ARL or U.S. Government. The U.S. Government is authorized to reproduce and distribute reprints for Government purposes notwithstanding any copyright notation herein. This work was performed in part under the auspices of the U.S. Department of Energy by Lawrence Livermore National Laboratory under Contract DE-AC52-07NA27344. HF also gratefully acknowledges the financial support of Natural Science Foundation of China (11302140).

Appendix A

Table A1. The bi-linear mobility law parameters used in the current simulations.

Slip plane	Dislocation character	Drag coefficient below transition velocity (10^{-6} pa s)	Transition velocity (km/s)	Drag coefficient above transition velocity (10^{-6} pa s)
Basal plane	Edge	4.68	1.83	81.25
	Screw	13.60	0.85	1625.0
Prismatic plane	Edge	8.25	1.61	125.0
	Screw	36.52	0.80	108.33
Pyramidal I plane	Edge	116.07	–	–
	Screw	–	–	–

Table A2. Dislocation decomposition at TB.*

Incident dislocation in matrix	Incident plane	Resulting dislocations in twin	Resulting planes	Number of twinning dislocations
$<a_1>=[2\bar{1}\bar{1}0]/3$	Ba (0001) Pr $(01\bar{1}0)$ PyI $(01\bar{1}\bar{1})$ PyI $(01\bar{1}1)$ Tp $(01\bar{1}2)$ Tp $(01\bar{1}\bar{2})$	$<a_1>=[2\bar{1}\bar{1}0]/3$	Depending on the power dissipation rule.	0
$<a_2>=[\bar{1}2\bar{1}0]/3$	Ba (0001) Pr $(10\bar{1}0)$ PyI $(10\bar{1}1)$ PyI $(10\bar{1}\bar{1})$ Tp $(10\bar{1}2)$ Tp $(10\bar{1}\bar{2})$	$0.5<c-a_1>=[\bar{2}113]/6$	Pr $(01\bar{1}0)$ PyII $(2\bar{1}\bar{1}2)$ PyI $(10\bar{1}1)$ PyI $(1\bar{1}01)$ Impenetrable Impenetrable	1
$<a_3>=[\bar{1}\bar{1}20]/3$	Ba (0001) Pr $(1\bar{1}00)$ PyI $(1\bar{1}01)$ PyI $(1\bar{1}0\bar{1})$ Tp $(1\bar{1}02)$ Tp $(1\bar{1}0\bar{2})$	$-0.5<c+a_1>=[\bar{2}11\bar{3}]/6$	Pr $(01\bar{1}0)$ PyII $(2\bar{1}\bar{1}\bar{2})$ PyI $(10\bar{1}\bar{1})$ PyI $(1\bar{1}0\bar{1})$ Impenetrable Impenetrable	−1
$<c+a_1>=[2\bar{1}\bar{1}3]/3$	Pr $(01\bar{1}0)$ PyI $(10\bar{1}\bar{1})$ PyI $(1\bar{1}0\bar{1})$ PyII $(2\bar{1}\bar{1}\bar{2})$	$-2<a_3>=2[11\bar{2}0]/3$	Ba (0001) PyI $(1\bar{1}01)$ PyI $(1\bar{1}0\bar{1})$ Pr $(1\bar{1}00)$	−2
$<c+a_2>=[\bar{1}2\bar{1}3]/3$	Pr $(10\bar{1}0)$ PyI $(01\bar{1}\bar{1})$ PyI $(1\bar{1}01)$ PyII $(1\bar{2}12)$	$0.5<c-a_3>+1.5<a_2>=[11\bar{2}3]/6+[\bar{1}2\bar{1}0]/2$	PyII $(11\bar{2}\bar{2})$ Pr $(10\bar{1}0)$ PyI $(01\bar{1}\bar{1})$ Ba (0001) PyI $(10\bar{1}\bar{1})$ PyI $(10\bar{1}\bar{1})$ Pr $(1\bar{1}00)$ Tp $(10\bar{1}\bar{2})$	−1

$<c+a_3>$ = $[\bar{1}\bar{1}23]/3$	Pr (1$\bar{1}$00)	$-0.5<c+a_3>+1.5<a_2>=[11\bar{2}\bar{3}]/6+[\bar{1}2\bar{1}0]/2$	Pr (1$\bar{1}$00) Tp (10$\bar{1}\bar{2}$)	–3
	PyI (01$\bar{1}$1)		PyI (01$\bar{1}$1) Ba (0001)	
	PyI (10$\bar{1}$1)		PyI (10$\bar{1}$1) PyI (10$\bar{1}$1)	
	PyII (11$\bar{2}$2)		PyII (11$\bar{2}$2) Impenetrable	
$<c-a_1>$ = $[\bar{2}113]/3$	Pr (01$\bar{1}$0)	$2<a_2>=2[\bar{1}2\bar{1}0]/3$	Ba (0001)	–2
	PyI (10$\bar{1}$1)		PyI (10$\bar{1}$1)	
	PyI (1$\bar{1}$01)		PyI (10$\bar{1}\bar{1}$)	
	PyII (2$\bar{1}\bar{1}$2)		Pr (10$\bar{1}$0)	
$<c-a_2>$ = $[1\bar{2}13]/3$	Pr (10$\bar{1}$0)	$-0.5<c-a_2>-1.5<a_3>=[\bar{1}2\bar{1}\bar{3}]/6+[11\bar{2}0]/2$	Pr (10$\bar{1}$0) Tp (1$\bar{1}$02)	–3
	PyI (01$\bar{1}$1)		PyI (01$\bar{1}$1) Ba (0001)	
	PyI (1$\bar{1}$0$\bar{1}$)		PyI (1$\bar{1}$0$\bar{1}$) PyI (1$\bar{1}$0$\bar{1}$)	
	PyII (1$\bar{2}$1$\bar{2}$)		PyII (1$\bar{2}$1$\bar{2}$) Impenetrable	
$<c-a_3>$ = $[11\bar{2}3]/3$	Pr (1$\bar{1}$00)	$0.5<c+a_2>-1.5<a_3>=[\bar{1}2\bar{1}3]/6+[11\bar{2}0]/2$	PyII (1$\bar{2}$12) Pr (1$\bar{1}$00)	–1
	PyI (01$\bar{1}\bar{1}$)		PyI (01$\bar{1}\bar{1}$) Ba (0001)	
	PyI (10$\bar{1}\bar{1}$)		Pr (1$\bar{1}$01) Pr (1$\bar{1}$01)	
	PyII (11$\bar{2}\bar{2}$)		PyI (10$\bar{1}$0) Tp (1$\bar{1}$02)	
$<c>$ = [0001]	Pr (1$\bar{1}$00)	$<a_2>-<a_3>=[\bar{1}2\bar{1}0]/3+[11\bar{2}0]/3$	Pr (1$\bar{1}$00) Tp (10$\bar{1}\bar{2}$)	–2
	Pr (01$\bar{1}$0)		Ba (0001) Ba (0001)	
	Pr (10$\bar{1}$0)		Tp (1$\bar{1}$02) Pr (10$\bar{1}$0)	

* Ba = basal plane, Pr = prismatic plane, PyI = pyramidal I plane, PyII = pyramidal II plane, Tp = twinning plane.

References

[1] A.A. Luo, J. Magnesium Alloy 1 (2013) 2.
[2] J.W. Christian, S. Mahajan, Prog. Mater. Sci. 39 (1995) 1.
[3] K.E. Prasad, K. Rajesh, U. Ramamurty, Acta Mater. 65 (2014) 316.
[4] E.W. Kelley, W.F. Hosford, Technical Report, 1967.
[5] M.R. Barnett, Z. Keshavarz, A.G. Beer, D. Atwell, Acta Mater. 52 (2004) 5093.
[6] L. Jiang, J.J. Jonas, A.A. Luo, A.K. Sachdev, S. Godet, Mater. Sci. Eng. A 445–446 (2007) 302.
[7] M. Knezevic, A. Levinson, R. Harris, R.K. Mishra, R.D. Doherty, S.R. Kalidindi, Acta Mater. 58 (2010) 6230.
[8] S.-G. Hong, S.H. Park, C.S. Lee, Acta Mater. 58 (2010) 5873.
[9] A.A. Salem, S.R. Kalidindi, R.D. Doherty, Acta Mater. 51 (2003) 4225.
[10] B. Wang, R. Xin, G. Huang, Q. Liu, Mater. Sci. Eng. A 534 (2012) 588.
[11] Z.S. Basinski, M.S. Szczerba, M. Niewczas, J.D. Embury, S.J. Basinski, Rev. Metall. 94 (1997) 1037.
[12] A.A. Salem, S.R. Kalidindi, R.D. Doherty, S.L. Semiatin, Metall. Mater. Trans. A 37 (2006) 259.
[13] D. Sarker, D.L. Chen, Scr. Mater. 67 (2012) 165.
[14] H. Fan, Z. Li, M. Huang, X. Zhang, Int. J. Solids Struct. 48 (2011) 1754.
[15] E. Van der Giessen, A. Needleman, Model. Simul. Mater. Sci. Eng. 3 (1995) 689.
[16] A. Arsenlis, W. Cai, M. Tang, M. Rhee, T. Oppelstrup, G. Hommes, T.G. Pierce, V.V. Bulatov, Model. Simul. Mater. Sci. Eng. 15 (2007) 553.
[17] H.M. Zbib, M. Rhee, J.P. Hirth, Int. J. Mech. Sci. 40 (1998) 113.
[18] L.P. Kubin, G. Canova, M. Condat, B. Devincre, V. Pontikis, Y. Brechet, Solid State Phenom. 23 and 24 (1992) 455.
[19] J.A. El-Awady, S. Bulent Biner, N.M. Ghoniem, J. Mech. Phys. Solids 56 (2008) 2019.
[20] H. Fan, Z. Li, M. Huang, Scr. Mater. 67 (2012) 225.
[21] C. Ouyang, Z. Li, M. Huang, H. Fan, Int. J. Solids Struct. 47 (2010) 3103.
[22] J.A. El-Awady, Nat. Commun. 6 (2015).
[23] Z. Li, C. Hou, M. Huang, C. Ouyang, Comput. Mater. Sci. 46 (2009) 1124.
[24] M. Huang, Z. Li, J. Tong, Int. J. Plast. 61 (2014) 112.
[25] H. Fan, S. Aubry, A. Arsenlis, J.A. El-Awady, Scr. Mater. 97 (2015) 25.
[26] H. Fan, Z. Li, M. Huang, Scr. Mater. 66 (2012) 813.
[27] C.C. Wu, P.W. Chung, S. Aubry, L.B. Munday, A. Arsenlis, Acta Mater. 61 (2013) 3422.
[28] G. Monnet, B. Devincre, L.P. Kubin, Acta Mater. 52 (2004) 4317.
[29] Z.H. Aitken, H. Fan, J.A. El-Awady, J.R. Greer, J. Mech. Phys. Solids 76 (2015) 208.
[30] G.S. Kim, Ph.D. thesis, University of Grenoble, 2011.
[31] L. Capolungo, I.J. Beyerlein, Z.Q. Wang, Model. Simul. Mater. Sci. Eng. 18 (2010) 085002.
[32] S. Olarnrithinun, S.S. Chakravarthy, W.A. Curtin, J. Mech. Phys. Solids 61 (2013) 1391.
[33] M.R. Barnett, Scr. Mater. 59 (2008) 696.
[34] A.M. Hussein, S.I. Rao, M.D. Uchic, D.M. Dimiduk, J.A. El-Awady, Acta Mater. 85 (2015) 180.

[35] J. Chevy, F. Louchet, P. Duval, M. Fivel, Philos. Mag. Lett. 92 (2012) 262.
[36] S. Aubry, V.V. Bulatov, M. Rhee, G. Hommes, A. Arsenlis, Model. Simul. Mater. Sci. Eng. (submitted for publication (2015)).
[37] H. Conrad, W.D. Robertson, Trans. Met. Soc. AIME 209 (1957) 503.
[38] R.E. Reed-Hill, W.D. Robertson, Acta Metall. 5 (1957) 717.
[39] A. Staroselsky, L. Anand, Int. J. Plast. 19 (2003) 1843.
[40] Y. Tang, J.A. El-Awady, Mater. Sci. Eng. A 618 (2014) 424.
[41] S. Groh, E.B. Marin, M.F. Horstemeyer, D.J. Bammann, Model. Simul. Mater. Sci. Eng. 17 (2009) 075009.
[42] J.A. Yasi, T. Nogaret, D.R. Trinkle, Y. Qi, L.G. Hector Jr., W.A. Curtin, Model. Simul. Mater. Sci. Eng. 17 (2009) 055012.
[43] H. Fan, J.A. El-Awady, Q. Wang, J. Nucl. Mater. 458 (2015) 176.
[44] Y. Tang, J.A. El-Awady, Acta Mater. 71 (2014) 319.
[45] S.R. Agnew, Ö. Duygulu, Int. J. Plast. 21 (2005) 1161.
[46] J. Zhang, S.P. Joshi, J. Mech. Phys. Solids 60 (2012) 945.
[47] J. Zhang, K.T. Ramesh, S.P. Joshi, Model. Simul. Mater. Sci. Eng. 22 (2014) 075003.
[48] P.B. Price, Proc. R. Soc. Lond. A Mater. 260 (1961) 251.
[49] M.H. Yoo, C-T. Wei, Philos. Mag. 14 (1966) 573.
[50] D.I. Tomsett, M. Bevis, Philos. Mag. 19 (1969) 129.
[51] J.I. Dickson, C. Robin, Mater. Sci. Eng. 11 (1973) 299.
[52] S. Lay, G. Nouet, Philos. Mag. A 70 (1994) 1027.
[53] M.H. Yoo, Trans. Met. Soc. AIME 245 (1969) 1841.
[54] A. Serra, D.J. Bacon, Acta Metall. 43 (1995) 4465.
[55] M. Yuasa, K. Masunaga, M. Mabuchi, Y. Chino, Philos. Mag. 94 (2013) 285.
[56] A. Serra, D.J. Bacon, Philos. Mag. A 73 (1996) 333.
[57] J. Wang, I.J. Beyerlein, C.N. Tomé, Int. J. Plast. 56 (2014) 156.
[58] C. Zhou, R. LeSar, Int. J. Plast. 30–31 (2011) 185.
[59] B. Li, S. Joshi, K. Azevedo, E. Ma, K.T. Ramesh, R.B. Figueiredo, T.G. Langdon, Mater. Sci. Eng. A 517 (2009) 24.
[60] S. Asgari, E. El-Danaf, S. Kalidindi, R. Doherty, Metall. Mater. Trans. A 28 (1997) 1781.
[61] Y. Xin, M. Wang, Z. Zeng, M. Nie, Q. Liu, Scr. Mater. 66 (2012) 25.
[62] H.J. Yang, S.M. Yin, C.X. Huang, Z.F. Zhang, S.D. Wu, S.X. Li, Y.D. Liu, Adv. Eng. Mater. 10 (2008) 955.
[63] C. Lou, X. Zhang, G. Duan, J. Tu, Q. Liu, J. Mater. Sci. Technol. 30 (2014) 41.
[64] J.H. Park, H.L. Kim, J.E. Jung, Y.W. Chang, Met. Mater. Int. 19 (2013) 389.
[65] A.J. Levinson, Ph.D. thesis, 2012.
[66] A. Ghaderi, M.R. Barnett, Acta Mater. 59 (2011) 7824.